The Meteoritical Society

Meteoritics & Planetary Science 43, Nr 12, 1917–1938 (2008)
Abstract available online at http://meteoritics.org

Validation of numerical codes for impact and explosion cratering: Impacts on strengthless and metal targets

E. PIERAZZO[1*], N. ARTEMIEVA[1, 2], E. ASPHAUG[3], E. C. BALDWIN[4], J. CAZAMIAS[5], R. COKER[6], G. S. COLLINS[7], D. A. CRAWFORD[8], T. DAVISON[7], D. ELBESHAUSEN[9], K. A. HOLSAPPLE[10], K. R. HOUSEN[11], D. G. KORYCANSKY[3], and K. WÜNNEMANN[9]

[1]Planetary Science Institute, 1700 E. Ft. Lowell Rd., Suite 106, Tucson, Arizona 85719, USA
[2]Institute For Dynamics of Geospheres, Russian Academy Sciences, Leninsky pr. 38, blg.1, Moscow 119334, Russia
[3]University of California Santa Cruz, Santa Cruz, California 95064, USA
[4]University College London, Gower St., London WC1E 6BT, UK
[5]University of Alabama, Birmingham, Alabama 35294, USA
[6]Los Alamos National Laboratories, Los Alamos, New Mexico 87545, USA
[7]Imperial College London, London SW7 2AZ, UK
[8]Sandia National Laboratories, P.O. Box 5800, Albuquerque, New Mexico 87185, USA
[9]Natural History Museum, Humboldt-University, Berlin 10099, Germany
[10]University of Washington, Seattle, Washington 98195, USA
[11]The Boeing Company, Seattle, Washington 98124, USA
[*]Corresponding author: E-mail: betty@psi.edu

(Received 24 March 2008; revision accepted 15 August 2008)

Abstract–Over the last few decades, rapid improvement of computer capabilities has allowed impact cratering to be modeled with increasing complexity and realism, and has paved the way for a new era of numerical modeling of the impact process, including full, three-dimensional (3D) simulations. When properly benchmarked and validated against observation, computer models offer a powerful tool for understanding the mechanics of impact crater formation. This work presents results from the first phase of a project to benchmark and validate shock codes. A variety of 2D and 3D codes were used in this study, from commercial products like AUTODYN, to codes developed within the scientific community like SOVA, SPH, ZEUS-MP, iSALE, and codes developed at U.S. National Laboratories like CTH, SAGE/RAGE, and ALE3D. Benchmark calculations of shock wave propagation in aluminum-on-aluminum impacts were performed to examine the agreement between codes for simple idealized problems. The benchmark simulations show that variability in code results is to be expected due to differences in the underlying solution algorithm of each code, artificial stability parameters, spatial and temporal resolution, and material models. Overall, the inter-code variability in peak shock pressure as a function of distance is around 10 to 20%. In general, if the impactor is resolved by at least 20 cells across its radius, the underestimation of peak shock pressure due to spatial resolution is less than 10%. In addition to the benchmark tests, three validation tests were performed to examine the ability of the codes to reproduce the time evolution of crater radius and depth observed in vertical laboratory impacts in water and two well-characterized aluminum alloys. Results from these calculations are in good agreement with experiments. There appears to be a general tendency of shock physics codes to underestimate the radius of the forming crater. Overall, the discrepancy between the model and experiment results is between 10 and 20%, similar to the inter-code variability.

INTRODUCTION

Impacts are a fundamental geologic process in the solar system. Over the years a vast amount of information has been obtained on crater morphology and ejecta emplacement from remote observations of impact craters on planetary surfaces. A complementary ground-truth data set on the crater subsurface structures has come from the geologic and geophysical investigation of terrestrial impact craters. However, these techniques can provide only partial information

regarding the dynamics of the impact process. The few known direct observations of solar system impact events in recorded history are those of the impact of comet Shoemaker-Levy-9 on Jupiter, the recent Deep Impact cratering of comet Tempel I, and various artificial impactors striking the Moon, such as SMART-1 and the upcoming LCROSS. Ongoing observations of Mars have shown that a dozen or more small impact craters formed over the past 20 years (Malin et al. 2007), but a direct observation of an impact event is still eluding us; large natural impact events are (fortunately) infrequent. In addition, the measures of the impactor are not generally known.

Laboratory impact experiments and studies of both laboratory and large field explosive cratering events have provided a limited window into the dynamics of impact cratering. Processes like shock melting and vaporization, which involve extreme pressures and temperatures, are not easily reproduced in tests using conventional explosives or typical laboratory scale impact experiments. Furthermore, the dominance of gravity in the later stages of crater formation implies that the results of small-scale laboratory and even kilometer-sized field tests cannot be safely extrapolated to the scale of the largest craters in the Solar System. Computer simulations provide the only feasible method for studying the formation of impact structures larger than about 1 km in diameter and for impact velocities typical of the solar system.

Modeling a complicated process like impact cratering requires sophisticated computer codes that can simulate not only the passage of a shock wave but also the behavior of geologic materials over a broad range of stress states and of deformation rates. Over the years numerical codes which solve the conservation of mass, momentum and energy equations simultaneously with constitutive relations for material properties have provided a significant tool for our understanding of impact processes. These codes are commonly referred to as shock codes or, anachronistically, as hydrodynamic computer codes, or hydrocodes, since they were first used to describe the hydrodynamic behavior of materials subjected to strong shocks (Anderson 1987). Even though the term “hydrocode” is the most commonly used in the literature, here we adopt the more appropriate term “shock code.” Today these codes can calculate the state variables of interest provided that adequate material models are available. They may have difficulties dealing with the discrete nature of matter (i.e., fragmentation or faulting), but this is an active area of research and there are methods to work around this. The rapid improvement of computer capabilities allows for increasing complexity in modeling impact cratering, opening the way for a new era of numerical modeling of the impact process, including fully three-dimensional (3D) simulations.

When validated against observation, computer models offer a powerful tool for understanding the mechanics of impact crater formation. Surprisingly, these highly developed codes are seldom systematically benchmarked and validated against existing laboratory and field data. Even when they are carried out (usually during code development or modification), benchmarking and validation studies are rarely openly available to the scientific community. As codes become more widely distributed, and access to computer power becomes more commonplace, this has resulted in an inefficient (and sometimes invalid) use of these codes in impact cratering studies. This paper presents the initial results of a widespread effort aimed at comparing (benchmarking) and validating shock codes.

NUMERICAL CODES

The foundations for modeling dynamic processes in any material are the equations describing the conservation of mass, momentum and energy. In addition, constitutive equations are necessary to describe the material response. All shock codes utilize similar forms of the conservation equations, but material models come in a wide variety of levels of sophistication. Constitutive equations are generally divided into two parts, one governing the material’s response in bulk (equation of state), and the other the response to the deviatoric deformations (strength). The conservation equations may be formulated using a coordinate system and calculation cells fixed in space, known as the Eulerian approach, or those moving with the material, known as the Lagrangian approach.

In the *Eulerian* approach, the mesh is fixed in space and the material flows through it. Historically, the limitation of this method is in the tracking of interfaces which leads to the averaging of materials in “mixed cells” of multiple materials and the averaging of state variables in single materials which have undergone advection. Various procedure have been developed over time to alleviate this problem; furthermore, adaptive mesh refinement (AMR) methods allow Eulerian codes to automatically generate localized high resolution regions (thus modifying the mesh size) in the model allowing much better interface and shock front tracking. AMR, however, requires the user to define the conditions for high resolution refinement, which is not always straightforward to do, and may lead to systematic errors.

In the *Lagrangian* approach the finite difference grid is fixed with the material, and deforms along with the material which trivially tracks interfaces. Generally, Lagrangian approaches are computationally more efficient. The major limitation of the Lagrangian approach is the inaccuracy of the numerical approximation when the cells are significantly distorted. Both approaches have been used in constructing shock codes, and both approaches can produce reliable and comparable results.

A hybrid method, referred to as *arbitrary Lagrange-Eulerian* (ALE) exists in which the computation remains Lagrangian until some condition is met at which point the material is allowed to advect while the mesh is transformed

dynamically according to user defined rules. Here Eulerian refers to the advection process; the mesh is not necessarily fixed over the duration of the simulation. This approach allows better tracking of interfaces without the cell distortion problem.

Meshless Lagrangian methods, such as Smoothed Particle Hydrodynamics (SPH), use interpolation nodes (i.e., particles) from which weighted functions ("kernels," representing parameters of interest) may be calculated. This approach removes the large deformation issues, since the particles are free to move, and is a valuable method for a problem which expands into a huge volume, since a grid-based code must model the total space. One of the main limitations of the SPH approach is its treatment of boundary conditions, which are more straighforwardly treated in gridded codes. It is also computationally expensive. Coupled versions of all these methods exist and some Lagrange codes allow the transformation of Lagrange cells into meshless Lagrange particles.

Material Models

Specific material properties govern the response of materials to stress, resulting in different behaviors of different materials for nominally the same impact conditions. The equations of state relate a material's instantaneous pressure, mass density and internal energy, and usually the temperature and entropy in addition. They define compressibility, thermal expansion, wave speeds, and other thermodynamic properties, and may also include descriptions of phase changes such as solid-solid, melt and vaporization. The deviatoric stresses determine the failure of the material according to common failure criteria. The equation of state description dominates the response in the early stages of the impact, when the stresses are very large compared to yield stress (i.e., deviatoric stresses are small compared to the pressures). But then having an accurate deviatoric model is critical for the modeling of the late stages of impact cratering where material strength determines the final shape and characteristics of the crater. The difficulty of building accurate material models remains the major problem for shock code modeling of impacts, and one that is receiving increasing attention. The simplest method, for instance defining a "fail pressure," or a single simple "strength" value, is proving to be inadequate for cratering problems, although more realistic methods place stricter requirements upon the computation of the deviatoric stress tensor in 3D.

Equations of State

The equations of state are unique for each material (they include all the complexities of its atomic, molecular, and crystalline structure), and describe its thermodynamic state over a wide range of pressures, internal energies (for impact computations), and specific volumes (or densities). One of the simplest examples of an equation of state is that of a perfect gas:

$$P = (\gamma - 1)\rho E \tag{1}$$

where P is pressure, E is internal energy, γ is the perfect gas constant and ρ is the gas density. The behavior of solids and liquids compressed by shock waves is, however, much more complex than this simple relation because of the strong interaction between the atoms (or molecules) of the medium. One of the simplest and most popular equations of state for solids is the Mie-Grüneisen equation of state, in which pressure and internal energy are separated into thermal and non-thermal components. It is based on a thermal component similar to that of a perfect gas ($P_T = \Gamma\rho E_T$), while the non-thermal components are associated to a reference state, also referred to as the 'cold' component (P_C and E_C, where $P_C = \Gamma\rho(E - E_C)$): $P = P_T + \Gamma\rho(E - E_C)$. The Grüneisen parameter $\Gamma(\rho)$ defines the pressure for a given internal energy per unit volume (Stacey 1977).

A widely used analytical equation of state was developed by Tillotson for high-speed impact computations (Tillotson 1962); however it provides no information about how to compute the temperature (which can be done using some assumptions, e.g., see Ivanov et al. 2002) or the entropy of a material and is unable to model melting and vaporization (some researchers estimate melt production in Tillotson by dividing the internal energy by a constant known as the melt energy, but this approach is not reliable; for instance, Tillotson has no latent heat of fusion).

More recent equations of state use increasingly complex descriptions that rely on different physical approximations and equations in different domains of validity. The best known example of these equations of state is ANEOS (Thompson 1970; Thompson and Lauson 1972), a semi-analytical model now used in a number of shock codes. In ANEOS pressures, temperatures, and densities are derived from the Helmholtz free energy and are, hence, thermodynamically consistent. Explicit treatment of melt and vapor is included. Although clearly superior to prior analytical equations of state, the original ANEOS has several limitations, such as the treatment of gases as monoatomic species, which causes it to overestimate the liquid-vapor phase curve and critical point of most complex materials. Complex materials are still difficult to model, especially when they involve several geologically relevant solid-solid phase transitions. An updated version of ANEOS is now available, which includes, among other things, the treatment of bi- and tri-atomic molecular gases (Melosh 2000, 2007). However, it does not address the problem of different complex molecules present in the vapor phase. ANEOS input parameters for several materials of geologic interest have been developed in the recent years, but much more work is still needed. PANDA (Kerley 1991) provides more options than ANEOS in the construction of multi-phase equations of

state in thermodynamic equilibrium (high-pressure polymorphs, solid-liquid, and liquid-gas coexistence lines, etc.), but at the expense of increased complexity that seems to preclude an active use of this equation of state model. With the exception of multi-phase calcite (Kerley 1989, 1991) no PANDA equations of state for rocks and minerals have been published in the open literature.

An important disadvantage in directly coupling complex codes like ANEOS and PANDA to shock codes is that they can be a significant time sink during cratering computations, and moreover can require special attention to compiler-related issues, sometimes holding back code implementation. A better approach in some cases is to use tabular equations of state. A classic example of this approach is SESAME, a well-known tabular equation of state database developed by the Los Alamos National Laboratory (e.g., Lyons and Johnson 1992) or the more recent database LEOS, used at the Lawrence Livermore Laboratory (Corey and Young 1998). But these tabular forms (at least in part) are often built using semi-analytical models, and thus suffer of the same limitations, including being restricted to limited ranges of the thermodynamic parameters. In particular, interpolation schemes between various regions of thermodynamic parameters often "smooth" away discontinuities in the equation of state, which can be a problem in particular at phase boundaries (see e.g., Swesty 1996). Independent tabular equations of state have been developed over the years for individual materials, such water ice (Ivanov 2005; Senft and Stewart 2008), taking advantages of a combination of available data and numerical codes. Detailed differences between different geological minerals and mixtures of minerals are still outside our ability to model.

Strength Models

Strength models describe the response of a material to stresses that induce deviatoric deformations, or changes of shape. The simplest strength models are for a perfectly elastic solid (Hooke's law): $\sigma = E\varepsilon$, where the stress σ is linearly proportional to the strain ε and for a Newtonian fluid where the stress is linearly proportional to the strain rate. A somewhat more complicated strength model is that of an elastic-perfectly plastic material, which is a good approximation of the stress response of many metals. A plastic material exhibits linear elastic behavior until a yield stress is reached, at which point the deviatoric stresses saturate. When the applied stress is reduced to zero (for example, after the shock wave has passed) the elastic strain is recovered, but the plastic strain remains. While this formulation was historically used to simulate the early stages of an impact event, today it is far too simplistic to model the behavior of geological materials, especially for the late stages of the impact.

Geological materials exhibit pressure, strain, strain-rate, and thermal effects. The strength of rock materials, measured by laboratory experiments (Lundborg 1968), has been approximated by a number of strength models developed for use in shock codes (e.g., Johnson and Holmquist 1994; Ivanov et al. 1997; Collins et al. 2004). Thermal effects on strength are often included by multiplying the yield strength at a given reference temperature by a simple function of internal energy (or temperature) which decreases monotonically from one at the reference temperature to zero at one chosen "melt" energy or temperature (ignoring the fact that the melt energy depends strongly on pressure.). Once the yield strength of a material is defined as a function of pressure, temperature, strain, etc., most strength models are based on the principle of comparing an invariant measure of stress in a cell (or at a point) with a yield strength; when the stress invariant measure exceeds the yield strength the stress tensor is modified to reduce the stresses to the yield limit, and permanent plastic deformation is accumulated. A brief explanation of the strength models used in this work to simulate the response of aluminum to deformation is provided in the Appendix. A general discussion of strength models for impact calculations is presented in Holsapple (2008).

Geologic materials are thought to fracture via faulting or fragmentation due to the activation, growth and coalescence of pre-existing cracks and flaws. Those processes are often modeled using a strain-rate dependent model such as the Grady-Kipp model (Grady and Kipp 1980). Those processes and their modeling often introduce phenomena of bulking (increased volume during fracture growth) and a degraded ability to withstand stress. The degradation of strength is often characterized by a damage parameter D which varies from zero (intact) to one (fully damaged, no tensile strength). That measure D can also used to modify the elastic moduli or stiffness measures of the material. Although strength algorithms have become quite sophisticated, there is seldom any data for their calibration, and these models can be very dependent on numerical resolution.

The Shock Codes Involved in the Tests

The shock codes that have been used in this first benchmarking test are described below:

ALE3D (Sharp 2004) is a 2D and 3D, Arbitrary Lagrange Eulerian, finite element code that treats fluid and elastic-plastic response of materials on an unstructured grid. It can be used for Eulerian calculations, where the remapping is done on the original mesh, or ALE calculations, where the remapping is done on an ideal grid (determined using an equipotential grid relaxation algorithm). The code was originally developed at the Lawrence Livermore National Laboratory.

AUTODYN (Century Dynamics, Inc. 2003) performs 2D and 3D simulations with multiple solution techniques, including Lagrange, Euler, ALE, and SPH (mesh-free), and various material models (predefined for many materials).

CTH (McGlaun et al. 1990) is a 1D-2D-3D Eulerian code developed at Sandia National Laboratories over several

decades. It has various features, such as AMR, extensive material models (predefined for many materials including explosives), explicit fracture mechanisms including void opening, multiple materials with interface tracking, and energy deposition. It can be run in several modes of geometry (rectangular, spherical, cylindrical).

iSALE/SALEB (Ivanov et al. 1997; Wünnemann et al. 2006) are code extensions to the SALE code (Amsden et al. 1980), an explicit arbitrary Lagrangian Eulerian finite difference code for calculating 2D (planar or cylindrical geometry) fluid flow at all speeds. The codes can model up to 3 materials and vacuum in any computation cell. A substantially revised 3D version iSALE-3D (Elbeshausen et al. 2007) has recently been developed based on the original SALE-3D code (Amsden and Ruppel 1981).

SAGE/RAGE (Gittings 1992) is an adaptive grid Eulerian code with a high-resolution Godunov scheme developed at the Los Alamos National Laboratory. It employs continuous AMR, and can be run in several modes of geometry (rectangular, spherical, cylindrical) and dimensionality (1D, 2D, 3D). RAGE also includes a separate module to model gray radiation diffusion (with non-equilibrium radiation and material temperatures).

SOVA (Shuvalov 1999) is an Eulerian code that can be run in different modes of geometry (planar, cylindrical, or spherical) and dimensionality (1D, 2D, 3D). It allows up to three different materials in any single cell. It also includes a procedure to describe particles' motion in an evolving ejecta-gas plume and their momentum-energy exchange (2-phase hydrodynamics) coupled to a size frequency distribution routine to model fragment sizes.

SPH (Benz and Asphaug 1994, 1995) was originally developed to simulate astrophysical processes (Lucy 1977; Gingold and Monaghan 1977), and has since then been modified to simulate solids, with the implementation of strength and fracture models as well as materials' equations of state (Tillotson and ANEOS). SPH is used in 1D, 2D and 3D.

ZEUS-MP2, originally built to model the behavior of gases in astrophysical situations (Hayes et al. 2006), has been modified for use in 2D and 3D Eulerian impact calculations (Korycansky et al. 2000, 2002; see Korycansky and Zahnle 2003 for the earlier version ZEUS-MP). Modifications include the implementation of models to treat solid materials such as the Tillotson equation of state and the p-alpha porosity model, (first presented in Herrmann 1969; corrected version in Carrol and Holt 1972) as well as Lagrangian tracer particles to provide density/temperature histories for individual mass elements. At present, a material strength model is not included in ZEUS-MP2.

BENCHMARK AND VALIDATION TESTS

Code validation is the process of testing results against known real-world situations. It differs from code *verification*, which is the process of demonstrating that the code solves the chosen physical equations, and solves them correctly. They would seem to be one and the same—a verified code should produce valid physical results—but the truth is that every code in our test has been carefully verified, yet they depart, sometimes significantly, in their solutions. This is a matter of the choices in material modeling, perhaps the accumulation of systematic errors that might apply to a particular problem—errors owing to under-resolved simulation, or physical regimes that strain the numerical accuracy (e.g., through too large of a time step), accumulated truncation errors, and so on. To evaluate and reliably apply the existing codes to various scientific problems it is necessary to know the code validity and reliability. When code results are questionable and untested, design of spacecraft missions and interpretations of laboratory, field and remote observations are necessarily vague. While code development is already happening in response to new requirements, all new models need testing and validation. Uniform validation for a suite of shock codes is required so that differences arising from the underlying numerical treatments can be distinguished from differences in the implementation of the material models. Furthermore, having several different code analyses of a given scenario is often the only metric we have for confidence in the results, especially since most scenarios are pushing us into new and non-validated regimes.

We have identified a series of standard tests for comparing and validating shock codes. They are divided into two categories: benchmark and validation tests.

Benchmark Tests

Benchmark testing involves the identification of impact standards: repeatable tests used to evaluate the performance of the codes in terms of accuracy, reliability and speed. It involves detailed comparisons of characteristic quantities that are not routinely measured in experiments. Simulations are divided into two classes.

- *Early-time simulations* focus on the early stages of the process, the propagation of a shock wave through the target and projectile. These simulations focus on maximum shock pressure, shock pressure decay, internal energy, temperature, melting/vaporization, and tracer particle histories during crater growth.
- *Late-time simulations* focus on the cessation of excavation and on the collapse of the impact crater. Here, a good strength model is important. Late-time model results determine the crater final morphology, tracer histories describing crater collapse, and stress/strain fields and their variations during late crater modifications.

Impact angle strongly affects the early stages of the impact, thus benchmark tests will involve vertical as well as 45° impact simulations to be carried out in 3D. We present here the results from the first benchmark tests, simple early-time simulations of aluminum into aluminum.

Validation Tests

Validation testing involves the evaluation of shock codes through comparison of simulations with a set of well-documented experiments that provide stringent tests of the physical models used in the codes. The experimental tests are drawn from laboratory studies of impact cratering and fragmentation and from large field tests of explosion cratering. Laboratory tests are useful because they are conducted under well-known conditions and provide direct information on impact events. However, they are necessarily conducted at small scales. Field explosion tests are complementary in that they encompass a much larger range of sizes and therefore provide a crucial test on strength models at size scales much larger than can be studied in the laboratory. When validating a code, it is important to consider as many aspects of the process as possible. A simulation must not only predict the correct final result, but also correctly reproduce the kinematics of the process, including material flow, ejection, and stress levels. Additionally, a simulation must use physically realistic models and parameters for equations of state and strength equations (including damage, fragmentation) of the materials involved in the tests. The experimental tests should be selected to encompass as many observables as possible and to sample a wide a range of experimental conditions. Here we present results from the first phase of our model validation, which involve materials that have a relatively simple constitutive behavior, such as water and metal.

BENCHMARK RESULTS

The first benchmark tests consist of early time simulations of an Al sphere 1 km in diameter impacting an Al target at 5 km/s and 20 km/s, vertically and at 45°.

Aluminum is a simple material with a well-known equation of state. Different equations of state models are used in the test runs, such as Tillotson, ANEOS, and SESAME and LEOS tables. These initial tests are designed to examine only the early stages of the impact process, so that no strength model is required. We use similar grids and Lagrangian tracer distributions for all the codes. The codes are compared in terms of spatial shock pressure decay and individual tracer pressure histories.

Inter-Code Variability

Figure 1 shows initial results of peak shock pressure decay in the target relative to the vertical impacts at 5 and 20 km/s. The peak shock pressure experienced by tracers located along a line downward from the impact point is shown with respect to the initial position of the tracers. The region close to the impact point is the contact and compression region, where the projectile releases most of the impact energy and momentum to the target. In this region, pressure decay with distance is small; thus it is sometimes called the isobaric core. Pierazzo et al. (1997) have shown that the size of this region slightly increases with impact velocity, and that the shock decay appears to be more pronounced at lower velocities. Using their normalized estimates for aluminum impacts, the downward extent of the contact and compression region is around 0.3 km for a 5km/s impact and around 0.5 km for a 20 km/s impact. Beyond the contact and compression region, the shock wave attenuates as it expands outwards. This is normally known as the pressure-decay region, occurring beyond about 1–2 projectile diameter (1 km) from the impact point. Here pressure and particle velocity decay rapidly with a power law of distance: $P = P_0(d/R)^n$, where d is the distance of the tracer from the impact point (material and the imbedded tracers are moved by the passage of the shock wave; however, at a distance of about 2 projectiles from impact point the motion of the tracer when the shock arrives is around 1% of the initial distance and becomes even smaller at farther distances). On a log-log plot of pressure versus distance the power law exponent, n, is provided by the slope of the decay. Understanding the decay behavior of the shock wave provides a way for evaluating important effects of impact cratering such as vaporization and melting, rock heating and fracturing. Previous work established that regardless of the target material, the shock decay depends on impact velocity, where the slope of the decay increases with increasing impact velocity (e.g., Ahrens and O'Keefe 1977; Bjorkman and Holsapple 1987; Pierazzo et al. 1997).

The code results for the two different impact velocities, summarized in Table 1, are as follows:

5 *km/s*. The average peak shock pressure estimated from tracers initially located out to about 200 m below the impact point (contact and compression region) for the codes that ran the 5 km/s vertical case is 40.4 ± 6.2 GPa (all the errors are 1-sigma values determined from the values relative to all the codes), ranging from a low of ~28.4 GPa estimated by ZEUS-MP to a high of ~48 GPa estimated by SOVA. The average slope in the pressure-decay region (2–6 km from the impact point in the case of this benchmark test) for the eight codes that ran the 5 km/s vertical variant is 1.2 ± 0.1, ranging from a minimum of 1.13 for iSALE and RAGE to a maximum of 1.41 for SPH. For example, about 4 projectile diameters away from the point of impact the average peak shock pressure (among all the shock codes) is 3.2 ± 0.5 GPa, with a minimum around 2.5 GPa (for SPH) to a maximum value around 4 GPa (for RAGE).

20 km/s. The 20 km/s vertical test simulation was run by six codes, and the average peak shock pressure out to about 600 m below impact (contact and compression region) is 379 ± 26 GPa, with a low of 335 GPa for ZEUS-MP to a high of 411 GPa for SOVA. The average slope of the pressure-decay region for the six codes that ran the 20 km/s vertical variant is 2.3 ± 0.1, ranging from a minimum of 2.27 for AUTODYN to a maximum of 2.53 for ZEUS-MP (Table 1).

Table 1. Benchmark results for the vertical (upper) and 45° (lower), 5 km/s and 20 km/s impacts of a 1 km diameter Al-sphere into aluminum. Each code is listed with the associated equation of state in parentheses. Columns for each impact velocity are mean shock pressure (P_{sh}) in the contact and compression region; pressure-decay slope (n), correlation (R) and number of points (between about 2 and 5 projectile diameters from the impact point). Overall mean values (at the bottom of each benchmark test case) are based on a linear average of values for the various simulations.

	5 km/s, vertical				20 km/s, vertical			
Shock code (EoS)	P_{sh} *(GPa) (0–300 m)*	*Slope, n*	*R*	*No. Points*	P_{sh} *(Gpa) (0–600 m)*	*Slope, n*	*R*	*No. Points*
ALE3D (*LEOS*)	39.2	1.35 ± 0.02	0.9997	20	381.1	2.38 ± 0.02	0.9988	32
AUTODYN-SPH (*Tillotson*)	41.3	1.307 ± 0.001	1	14	396.4	2.269 ± 0.003	0.9999	25
CTH (*ANEOS*)	44.5	1.31 ± 0.04	0.995	13	380.3	2.382 ± 0.009	0.9996	54
iSALE (*Tillotson*)	42.7	1.13 ± 0.01	0.9992	19	371.2	2.30 ± 0.02	0.9987	32
RAGE (*SESAME*)	35.5	1.13 ± 0.01	0.9992	12				
SOVA (*ANEOS tables*)	48.0	1.207 ± 0.006	0.9998	21	411.1	2.28 ± 0.01	0.9998	13
SPH (*Tillotson*)	43.5	1.41 ± 0.01	0.9997	12				
ZEUSMP (*Tillotson*)	28.4	1.19 ± 0.01	0.9990	17	334.7	2.53 ± 0.01	0.9997	21
Mean	40.4 ± 6.2	*1.2 ± 0.1*			379 ± 26	*2.3 ± 0.1*		
	5 km/s, 45°				20 km/s, 45°			
	Direction	*Slope, n*	*R*	*No. points*		*Slope, n*	*R*	*No. points*
ALE3D	*0°*	1.226 ± 0.007	.9996	23		1.95 ± 0.01	0.9993	26
(*LEOS*)	*45°*	1.18 ± 0.03	0.9978	11		2.46 ± 0.01	0.9998	15
iSALE3D	*0°*					1.53 ± 0.02	0.9991	16
(*Tillotson*)	*45°*					2.304 ± 0.009	0.9999	16
RAGE	*0°*	1.112 ± 0.004	0.9998	28		1.06 ± 0.02	0.9984	16
(*SESAME*)	*45°*	1.318 ± 0.009	0.9996	20		1.11 ± 0.03	0.9966	10
SOVA	*0°*	1.12 ± 0.03	0.9970	11		1.635 ± 0.006	0.9999	22
(*ANEOS tables*)	*45°*	0.96 ± 0.01	0.9989	11		2.188 ± 0.007	0.9999	14
ZEUS-MP	*0°*	0.90 ± 0.02	0.9977	13		1.51 ± 0.03	0.9975	15
(*Tillotson*)	*45°*	0.87 ± 0.03	0.9909	14		2.57 ± 0.02	0.9995	16
Mean	*0°*	*1.1 ± 0.1*				*1.5 ± 0.3*		
	45°	*1.1 ± 0.2*				*2.1 ± 0.6*		

As a side note, the average peak shock pressure in the contact and compression region for both simulations is below the planar shock approximation limit (~60 GPa for the 5 km/s case and 522 GPa for the 20 km/s case, using the Al parameters for the linear shock-particle velocity relation from Table AII.2 of Melosh 1989), which is expected due to the rather different geometry of the problem (furthermore, no tracers were located exactly at the impact point).

Some of the 3D codes involved in this testing exercise were used to run oblique simulations (ALE3D, iSALE3D, RAGE, SOVA, ZEUS-MP). In oblique impacts the shock wave near the impact point becomes asymmetric, causing the contact and compression region to be skewed in the downrange direction (Pierazzo and Melosh 2000). This is shown in Fig. 2 which shows shock pressure decay in the target along a line parallel to the surface (60 m or 3 cells below) downrange of the impact point (see, Fig. 2a for the schematic of the tracers distribution) for the 45° impacts of an aluminum sphere 1 km in diameter on an aluminum target at 5 km/s (Fig. 2b) and 20 km/s (Fig. 2c). The maximum shock pressure does not occur directly below but roughly a projectile radius downrange of the impact point. Figure 3

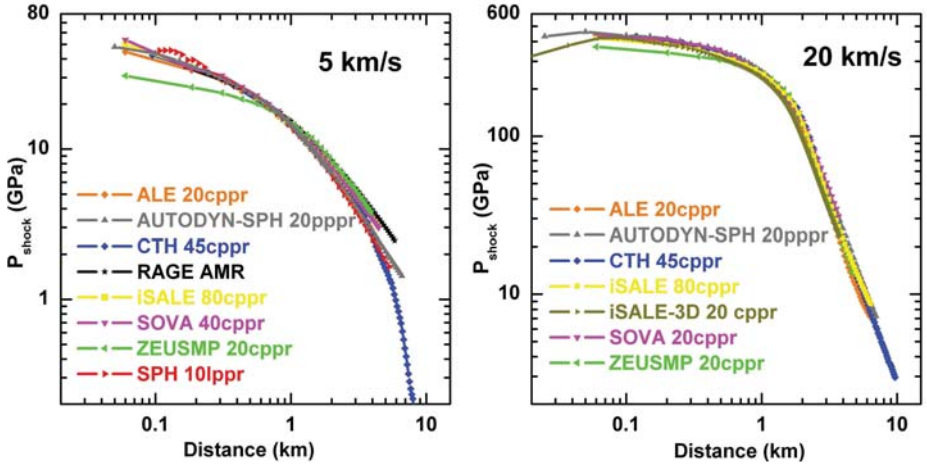

Fig. 1. Shock pressure decay downward from the impact point for a 1 km diameter aluminum sphere impacting an aluminum target at 5 km/s and 20 km/s respectively. Resolution is in cells per projectile radius, cppr; for SPH we define slppr, smoothing length per projectile radius (where the smoothing length for particle interaction is used instead of cell size) or pppr, particle length per projectile radius (used in AUTODYN).

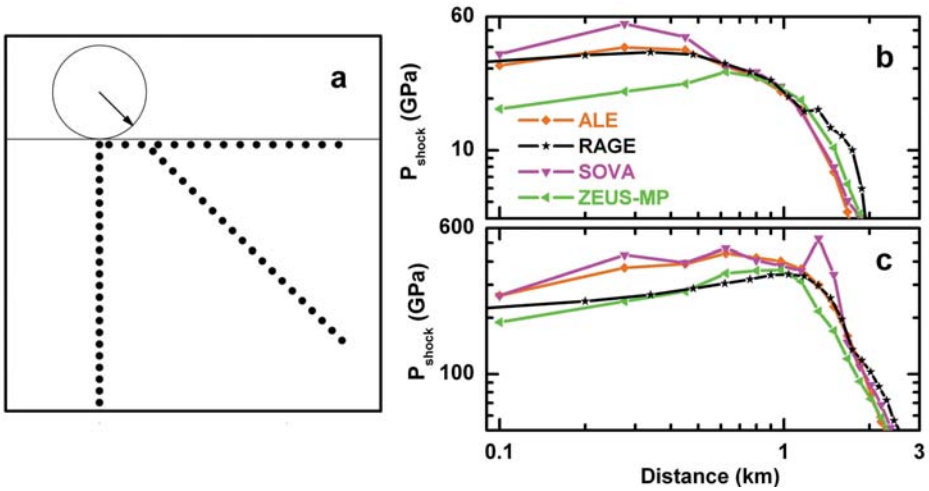

Fig. 2. a) Schematic of Lagrangian tracer distribution used to illustrate shock decay in the target for the 45° impacts of aluminum into aluminum at 5 and 20 km/s. Shock pressure decay away from the impact point (parallel to surface) are shown b) for 5 km/s and c) for 20 km/s.

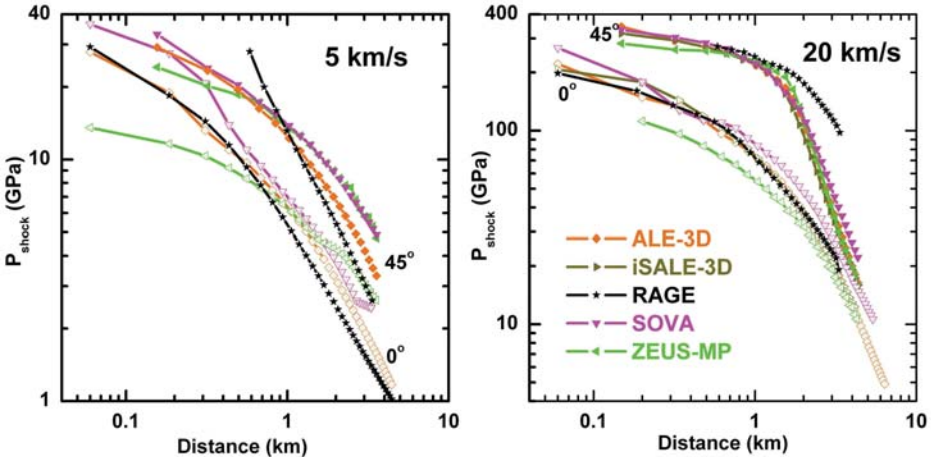

Fig. 3. Shock pressure decay downward from the impact point (open symbols) and at 45°, one projectile radius downrange (solid symbols; $d = \sqrt{(x - R_{pr})^2 + z^2}$) for a 1 km diameter aluminum sphere impacting at 45° an aluminum target at 5 km/s and 20 km/s.

shows pressure decay in the plane of impact, both directly downward from the impact point (the classic direction for pressure decay estimates in vertical impact simulations) and at 45° from the surface but starting from about one projectile radius downrange of the impact point, as shown in Fig. 2a. The pressure decay region in the two directions is characterized by similar slopes in the 5 km/s case, (1.1 ± 0.1) consistent with the pressure decay slope of the vertical test. In the 20 km/s test, the downward slope is shallower (1.5 ± 0.3) than the slope of the 45º pressure decay (2.1 ± 0.6) and the pressure decay slope of the vertical test (2.3 ± 0.1).

Differences among the various codes are to be expected and are within 15% and 8% for the 5 km/s and 20 km/s simulations respectively. They can be due to a number of causes related to code set up. Obvious causes include variation in mesh size and cell size (resolution); less transparent causes are variation in artificial parameters like artificial viscosity settings or Courant time step controllers. Finally, material models, in particular equations of state for early time simulations, can also affect the output.

Code Convergence: Resolution Effect

To test potential effects of mesh resolution within codes, most of the codes ran the 5 km/s vertical impact simulation at various resolutions, ranging from 5 cells-per-projectile-radius (cppr) to 45 cppr (i.e., all cells in the mesh have the same size, given by the ratio of the projectile radius to the resolution used: 5, 10, 20, 40, and 45), and for certain codes to the use of AMR (where the mesh resolution changes in space and time to resolve regions of interest). For these tests this corresponds to a cell size of 100 m down to 12.5 m or smaller for the minimum cell size in the adaptively refining mesh. Lower resolution implies larger cell sizes for the same physical dimensions of simulation mesh. Calculated impact related parameters (velocity, pressure, temperature, density, etc.) are averaged over the cell volume, thus the larger the cell, the less accurately the parameters represent a specific location in the target. Figure 4 shows the effect of resolution on the simulation results for the 5 km/s vertical impact test. Table 2 provides estimates of code differences (in percentage from the higher resolution) for the regions near the impact and in the pressure decay region. The results suggest that most of the codes converge for resolutions of 20 cppr or higher, although a resolution of 10 cppr still provides reasonable results. On average, when compared to 40 cppr or higher, a resolution of 20 cppr appears to underestimate peak shock pressures by at most 10%. Differences in resolution simulations appear to be less marked in the region near the impact (up to 1.5 projectile radii from impact), where the 20 cppr resolution appears to underestimate peak shock pressure by a few percent, than in the pressure-decay region.

Individual codes appear to have slightly different responses to changes in resolution from the near impact (up to 1.5 projectile radii from impact) to the pressure-decay (from about 2 to 10 projectile radii from impact) regions. For example, ALE3D (especially for ALE calculations) appears to perform well even at the lowest resolution tested, 10 cppr, with variations on average well below 10%. Only one code, ZEUS-MP, ran the 5 cppr case, which clearly provides artificially low estimates of shock pressure.

Limited resolution simulations for the 20 km/s vertical impact test are available only for a few codes (iSALE, ZEUS-MP, SOVA). Overall, the results indicate a more pronounced difference among different resolution simulations than in the 5 km/s case. However, the convergence for resolution of 20 cppr or higher appears to hold.

Effect of Artificial Viscosity

Artificial internal parameters are included in any code used to model strong shocks (e.g., Anderson 1987) and are necessary for code stability; in other words, to ensure that the calculated results are physical. Artificial viscosity is introduced to suppress unphysical pressure oscillations behind a shock wave that are a consequence of numerically representing an abrupt change in pressure. This is achieved by "smoothing" the (theoretically instantaneous) change in pressure over a few cells. Although "artificial" in nature, this term can be associated with small-scale processes, i.e., processes that occur at scales smaller than one cell size and cannot otherwise be resolved in the computation. The term is commonly divided into two components: a quadratic and a linear term, as described in Anderson (1987). Both terms contribute to the smoothing of the shock wave, and can be used together or individually. Unfortunately, the use of high viscosity may also increase the amount of heating from the shock wave, thus affecting the overall simulation outcomes (particle velocity, temperatures, etc.). Therefore, care must be used when using this parameter.

Normally, artificial viscosity is not a parameter that modelers modify during the initialization of model runs, although it can have a noticeable effect on the results. Rather, it is provided as an internal parameter, which is rarely modified by users. Figure 5 shows the effects of varying artificial viscosity on the results from simulations run with SOVA. The code includes two artificial viscosity components (see Shuvalov 1999 for more details) analogous to the quadratic and linear terms described in Anderson (1987). The use of a simple quadratic term spreads the shock over 3 cells, and partially smoothes the artificial oscillations in the shock, as shown in Fig. 5b. The addition of a linear component contributes to an even smoother shock, and overall lower estimates of the maximum peak shock pressures for the various tracers. Simulations without artificial viscosity can produce strong artificial amplitude oscillations at the shock discontinuity, resulting in unrealistic maximum peak shock pressures (like in the "no viscosity" case in Fig. 5, where the maximum peak pressure of ~75 GPa is higher than the planar approximation estimate of around 60 GPa). In SOVA, the systematic offset in maximum peak shock pressures (from the

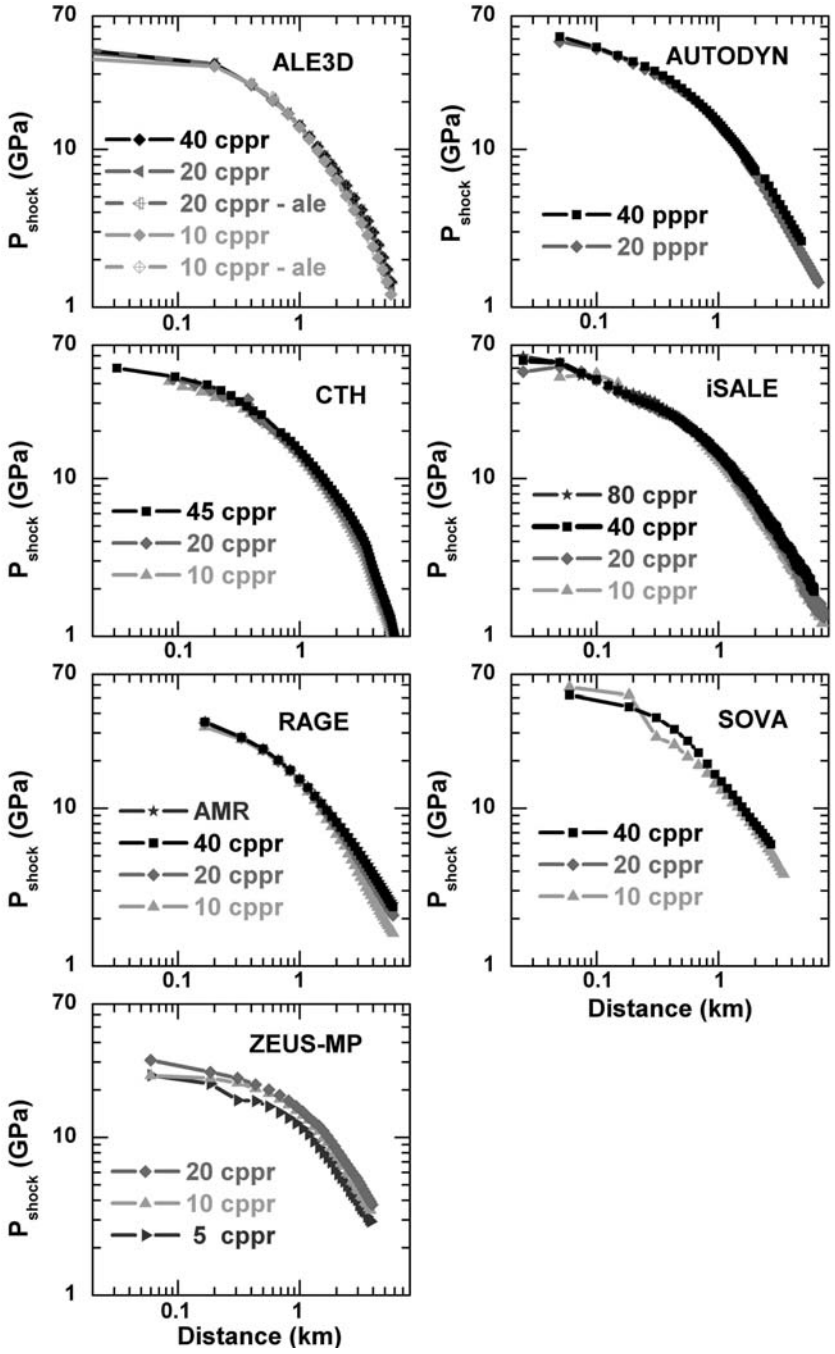

Fig. 4. Resolution effects relative to the simulation of a 1 km diameter aluminum sphere impacting vertically an aluminum target at 5 km/s for the various codes involved in the benchmark tests.

smoothest case, linear + quadratic viscosity) for the various tracers (Fig. 5a) in the downward direction is around 30% (with peaks of over 60%) for the run with no artificial viscosity, and 18% for the run with only quadratic viscosity.

VALIDATION RESULTS

Water tests are relatively simple. Simulations of impacts and explosions in water do not need a strength model, but gravity needs to be included to model the late stages of crater growth. Our first validation test consists in modeling a Boeing quarter space laboratory experiment of a glass sphere, 2 mm in diameter, impacting water at 4.64 km/s (Schmidt and Housen 1987). This experiment used a "quarter-space" rectangular box made from 1.25 cm thick Al, 76 cm × 38 cm × 23 cm in size, with a 5-cm thick plexiglass window inserted close to the impact point for viewing purposes, as shown in Fig. 6. The container was not affected by the test (no visible

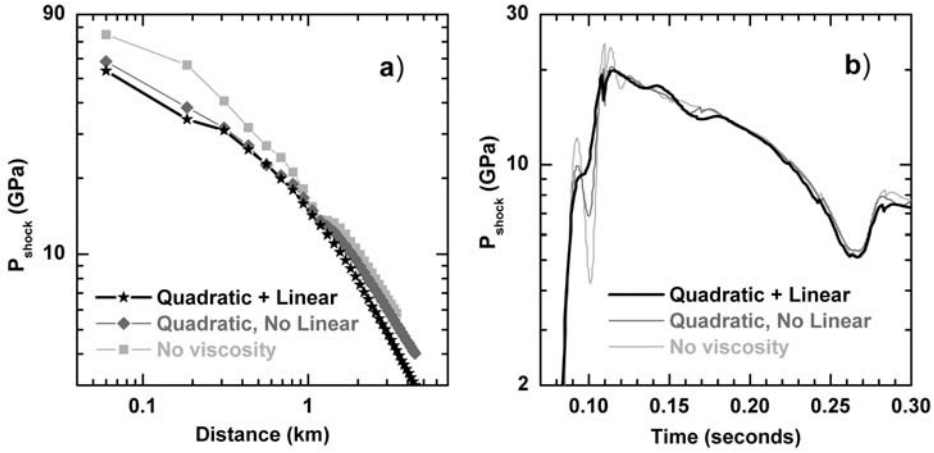

Fig. 5. SOVA simulation of a 1 km diameter aluminum sphere impacting an aluminum target at 5 km/s. a) Shock pressure decay in the target, downward from the impact point, and b) shock wave profile for a mid-distance tracer (6th from impact point, at an initial distance of 0.685 km from the impact point), for various artificial viscosities.

Table 2. Results of the resolution study for the 5 km/s vertical impact simulation in the near impact and pressure decay region (parentheses report the spatial extent of the region). Values list average difference in peak shock pressures between two resolutions (R1–R2) in percent: $100^{*}(p_{R1} - p_{R2})/p_{R1}$.

Code	Resolution (cppr)	Near-impact $(0–1.4)R_{pr}$	Pressure-decay $(2–10)R_{pr}$
AUTODYN	40-20	3.1 ± 1.7	10.0 ± 5.9
ALE3D	40-20	0.03 ± 0.03	4.6 ± 2.3
	40-20ale	0.1 ± 1.4	0.93 ± 0.91
	20-10	0.6 ± 2.7	8.2 ± 4.0
	20-10ale	0.3 ± 3.4	2.6 ± 3.4
	20ale-10ale	0.3 ± 2.2	6.2 ±4.9
	10ale-10	0.9 ± 2.6	5.6 ± 1.6
	20ale-20	0.04 ± 1.31	3.7 ± 2.0
CTH	45-20	3.0 ± 5.8	9.3 ± 1.9
	20-10	1.7 ± 8.8	20.7 ± 2.5
iSALE	80-40	3.0 ± 2.9	1.2 ± 3.0
	40-20	2.0 ± 1.6	4.7 ± 5.1
	20-10	1.5 ± 6.3	10.4 ± 3.9
RAGE	AMR-40	0.1 ± 0.4	3.0 ± 0.9
	40-20	0.8 ± 0.5	7.9 ± 3.3
	20-10	3.0 ± 2.1	16.1 ± 6.8
SOVA	40-20	1.9 ± 3.1	5.8 ± 3.0
	20-10	5.9 ± 23.1	6.5 ± 1.4
ZEUSMP	20-10	8.5 ± 5.8	9.9 ± 2.8
	10-5	13.9 ± 8.3	18.6 ± 2.1

signs of deformation). Ambient chamber pressure was around 3400 Pa (above the vapor pressure, which is ~2300 Pa at room temperature). Diagnostics measured during the experiment were crater profile at given times (up to 83 ms), and ejection velocities of a few small plastic beads floating on the surface. Experimentally determined crater radius and depth (measured at the pre-impact surface) over time are provided in Table 3. Based on high-speed films of the impact, the beads appeared to move at the same speed as the water and so provide a good representation of the water ejection velocity field.

Table 3. Experimental data for the glass-on-water laboratory impact (validation #1), where t_{exp} is the time at which crater radius (R_{exp}) and depth (D_{exp}) were measured.

t_{exp} (ms)	R_{exp} (cm)	D_{exp} (cm)
0.191	1.608	2.35
0.382	2.297	2.6
0.764	2.963	3.32
1.146	3.423	3.85
1.91	4.112	4.61
3.436	5.031	5.39
5.72	6.064	6.41
9.516	7.098	7.514
15.18	8.316	8.83
22.666	9.487	9.7
31.9	10.636	10.602
44.553	11.807	11.46
65.334	13.3	12.1
83.187	14.357	12.054

The quarter-space technique, while providing valuable information on crater growth and the impact-induced flow field, is not perfect in the sense that some of the impact energy is absorbed into the viewing window. For sand targets, the end result is that the final crater radius in a quarter-space test is typically about 10% smaller than that from an equivalent test in an semi-infinite half-space. This reduction in crater radius appears to roughly hold for water impacts as well, based on comparisons of the quarter-space water impact experiment with data reported by Gault and Sonnett (1982) for impacts into half-space water targets.

Aluminum is another simple material that has been used in many experiments and has well-known properties both in terms of equation of state and material strength. For our second validation test we choose to model laboratory

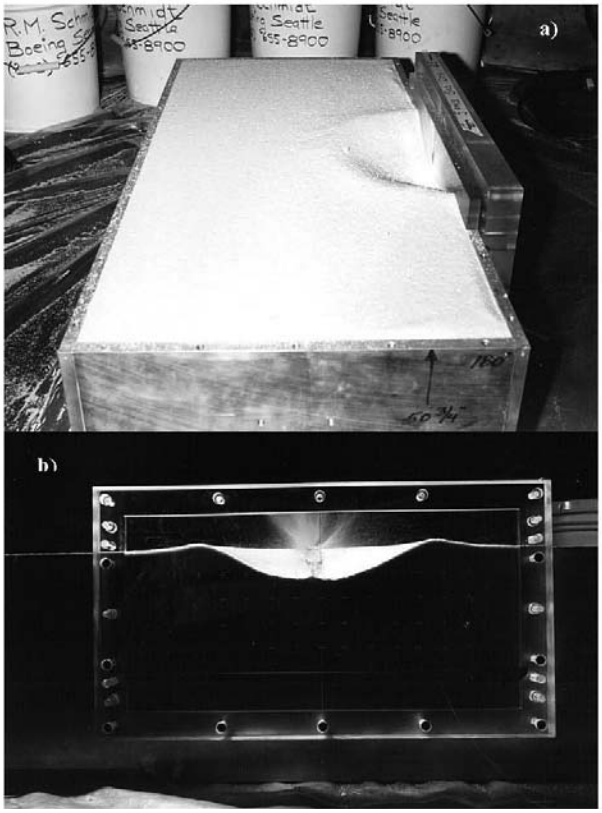

Fig. 6. Quarter space tank (here shown for a sand impact) used in the glass-on-water impact experiment modeled by shock code simulations. The container is an aluminum quarter-space rectangular box made of 1.25 cm thick Al, 76 cm × 38 cm × 23 cm in size (shown in a). The impact side has a thick glass window for viewing purposes (frontal view shown in b).

experiments of an aluminum sphere (Al 2017-T4), 6.35 mm in diameter, impacting perpendicularly at about 7 km/s onto various aluminum alloy cylinders (few tens of millimeters in thickness and diameter, large enough to be considered 'quasi-infinite' in the experiment; Prater 1970). In the experiments, material strength was varied by employing targets of 1100-O, 6061-T6, and 7075-T6 and -T0 aluminum alloys. Flash X-ray techniques were used to measure accurately the rate at which the crater grew during the impact process. Table 4 provides crater radius and depth over time for the Al 1100-O and Al 6061-T6 targets, which have been modeled here. Four separate X-ray heads were positioned circumferentially around the target to image the transient crater at four separate times. The X-ray images provided cross-sectional views of the crater. Depth and radius during crater growth were measured with a divider by viewing the X-ray films on a variable intensity light table. An absolute length calibration was made from additional X-ray images of the final crater taken after the event. Based on repeated measurements by different analysts, the measurement error on crater dimensions (see Table 4) was estimated to be ±0.5 mm to ±1 mm, depending on image quality.

The simulations were carried out assuming an arbitrarily large mesh (see tables). Fixed input conditions included the projectile size, impact velocity/angle, shape and material (glass, aluminum), target material (water, aluminum alloys), and mesh size. Technical details (including resolution), material models and relative parameters for the materials were chosen by individual modelers and are reported in Tables 5 and 6. The strength models used were: von Mises, Johnson-Cook and Steinberg-Guinan (see Appendix). This approach is clearly different from the benchmark testing. Benchmark tests focus on comparing code performances given simple ideal tests. Validation tests are also about testing the modelers' identification and use of the proper models. Our main goal in this context is to verify how modelers' choices can affect the output results. Understanding the fundamental cause(s) of the differences between the various codes, while ideal, requires a much more intensive and systematic work that is beyond the scope of this study.

Validation #1: Glass Sphere into Water

The glass-into-water simulation was computationally challenging. For this impact, the crater radius after 83.2 ms (the last time the crater dimensions were recorded in the experiment, and the time at which the crater reached its maximum depth) was 14.3 cm. Hence, the computational domain required to cover the entire region of interest was more than 70 times larger than the 2 mm projectile diameter. To perform an impact calculation on such a large mesh without the capability of dynamically modifying the spatial resolution requires a large amount of memory and, more significantly, a long calculation time. In this case, codes with some form of adaptive mesh refinement or re-gridding technology have a significant advantage in simulating the glass-into-water impact experiment in its entirety. All the other codes tested were forced to use a relatively low resolution (5–10 cppr) to carry out a significant portion of the experimental test in a reasonable computation time.

In the early stages of impact, where results for a number of codes are available, the model results appear to follow the experimental data quite closely, as shown in Fig. 7. A brief investigation of the early evolution (<3.5 ms) of crater radius and depth with time (Fig. 8) shows variability in the model results compared to the experiments of less than 15% (except for SOVA, which reaches 25%, and ZEUS-MP2, which reaches 50%). The full coverage of the validation test is available for three codes: ALE3D, CTH, and ZEUS-MP2, with iSALE covering about half of the experiment duration. Only one time step is available for AUTODYN (not enough for an assessment of its performance). Generally, the codes tend to underestimate the experimental crater diameter and depth. The effect is more marked than shown in Figs. 7 and 8, considering that the quarter-space results tend to underestimate the "true crater" size by about 10%, at least for

Table 4. Experimental data for the aluminum-on-aluminum laboratory impact (validation #2), where t_{exp} is the time at which crater radius (R_{exp}) and depth (D_{exp}) were measured.

Target = Aluminum 6061-T6				Target = Aluminum 1100-O			
t_{exp} (ms)	R_{exp} (cm)	t_{exp} (ms)	D_{exp} (cm)	t_{exp} (ms)	R_{exp} (cm)	t_{exp} (ms)	D_{exp} (cm)
2.845	0.7505	2.872	0.825	0.971	0.6345	3.075	0.803
3.082	0.8475	2.633	0.825	3.083	0.7555	2.994	0.905
5.098	0.8835	4.787	0.869	2.863	0.776	5.607	0.976
5.216	1.0255	6.582	1.066	5.528	0.857	5.265	1.004
6.402	1.048	6.462	1.125	4.986	0.922	7.670	1.154
6.639	1.0505	9.334	1.213	6.418	1.057	9.948	1.282
8.180	1.0685	7.779	1.256	7.348	1.0905	10.297	1.273
6.758	1.1065	14.121	1.293	8.709	1.068	15.082	1.522
7.943	1.1065	14.839	1.293	8.841	1.106	18.871	1.616
9.721	1.111	25.25	1.304	12.314	1.207	23.497	1.762
7.825	1.1405	27.04	1.295	15.08	1.2585	26.668	1.765
9.247	1.1855	40.808	1.281	16.151	1.3525	27.024	1.779
14.226	1.2215	43.68	1.245	18.658	1.3365	31.261	1.815
16.716	1.251	52.176	1.322	23.618	1.437	38.412	1.781
15.412	1.278	68.81	1.324	24.683	1.5175	40.658	1.837
17.427	1.3255			26.634	1.535	52.391	1.819
22.051	1.3415			26.42	1.569	65.660	1.842
25.726	1.3595			26.779	1.605	67.416	1.822
27.149	1.346			26.436	1.605	73.985	1.799
27.741	1.314			28.844	1.6225	79.973	1.804
27.741	1.3095			31.108	1.5725		
37.344	1.2985			36.871	1.6815		
39.952	1.355			38.229	1.6525		
40.664	1.366			40.614	1.6185		
40.901	1.3435			43.831	1.656		
43.865	1.33			46.357	1.6825		
44.102	1.321			52.621	1.6345		
44.932	1.2895			58.696	1.6735		
43.983	1.242			62.999	1.5855		
47.895	1.33			65.642	1.6165		
51.452	1.249			67.48	1.6385		
52.4	1.2645			65.672	1.615		
58.684	1.2805			74.098	1.652		
69.235	1.321			79.601	1.685		
72.673	1.267						

late times. Simulations with ALE-3D, CTH, iSALE, RAGE, and SOVA appear to follow the experimental data quite closely. Early simulations with SOVA and RAGE had significant problems which were successfully tracked down. The SOVA simulation was initially carried out with a very small mesh and it began to strongly underestimate crater size as the crater profile approached the edges of the mesh. The initial RAGE simulation was carried out using a 1 atm atmosphere over the water, which caused the crater shape to eventually deviate strongly from what observed in the experiment (as a side note, the crater shape was instead a very good fit to similar experiments in water with a normal atmosphere). Minor effects may have been due also to the initial choice of boundary conditions and resolution, as well as the initial choice of viscosity. The simulation with ZEUS-MP2 seems to develop instabilities beyond 2 ms, which have affected the simulation results. Possible difficulties contributing to the results seen with ZEUS-MP2 for this test could be due to pressure-wave reflections at the boundaries in the target region, problems with interactions of free surfaces, material interfaces, and rarefaction waves. The use of an atmosphere above the surface may also have affected the simulation (as for the RAGE case). No clear conclusion has been reached yet. It may be that the modified ZEUS-MP2, derived from a purely Eulerian gas-dynamics code, is poorly suited to this particular type of problem. As noted above, all the ZEUS-MP2 modifications for impact problems on solid surfaces were made by one of the authors (Korycansky) and his collaborators.

Intra-Code Variability

The availability of two different resolution simulations with iSALE for the glass-on-water experiment allows us to once again illustrate the importance of resolution, not only in

Table 6. Summary of various shock codes set up for the aluminum-on-aluminum impact simulations.

Code	Simulation type	Strength model used (see Appendix)	Mesh size	Resolution (cppr)	Boundary conditions
AUTODYN	2D(SPH)	Steinberg-Guinan strength model[1] *Al 1100-O*: G_o= 27.1 GPa;Y_0 = 40 MPa; Y_{max}= 480 MPa; β = 400; n = 0.27;G'_p = 1.767; G'_T = –16.69 MPa; Y'_p = 0.002608; T_m = 1220 K *Al 6061-T6* (ρ = 2.703 g/cm^3): Go = 27.6 GPa;Y0 = 290 MPa; Y_{max} = 680 MPa; β = 125; n = 0.21; G'_p = 1.8; G'_T = –17 MPa; Y'_p = 0.018908; T_m = 1220 K	*r*: 0 to 75 cm *z*: –75 to 7 cm	10 (pppr)[2]	Rigid (reflecting)
CTH (KH)	2D	Johnson-Cook plastic model[3] *Al 1100*: A = 49 MPa; B = 157 MPa; C = .016; M = 1.7; n = 0.167; T_{rf} = 800 K; Poisson = 0.3 + rate effects *Al 6061*: A = 244 MPa; B = 488 MPa; C = 0; M = 3; N = 0.5; T_{rf} = 800 K	*r*: 0 to 50 cm (0 to 5 cm - ST[4]) *z*: –50 to 5 cm (–4 to 1 cm - ST[4])	AMR: max 48 cppr	Rigid (reflecting)
RAGE	2D	Steinberg-Guinan strength model for target[5] (projectile is strengthless)	*r*: 0 to 110 cm *z*: –70 to 70 cm	20	Side/bottom: reflecting Top: outflow
iSALE	2D	Von Mises Strength Model *Al 6061*: Shear strength, $(\sigma_1-\sigma_3)/2$ = 207 MPa[6]; Y_{vm} = 414 Mpa Johnson-Cook plastic model *Al 6061(JSC1)*[3]: A = 244 MPa; B = 488 MPa; C = 0; m = 3; n = 0.5; T_{rf} = 800 K *Al 6061(JSC2)*[7]: A = 324 MPa; B = 114 MPa; C = 0.002; m = 1.34; n = 0.42; T_{rf} = 800 K *Al 1100*[3]: A = 49 MPa; B = 157 MPa; C = .016; m = 1.7; n = 0.167; T_{rf} = 800 K	*r*: 0 to 7 cm *z*: 2 to 7 cm	10, 20, 40	Top: outflow Bottom: no slip Sides: free slip

[1]Steinberg-Guinan model parameters taken from the AUTODYN library.
[2]pppr = particles per projectile radius.
[3]Johnson-Cook model parameters derived from fits to experimental data in Benck et al. (1976).
[4]ST = small target.
[5]Steinberg-Guinan model parameters taken from Steinberg (1996).
[6]Strength data obtained from http://asm.matweb.com/search/SpecificMaterial.asp?bassnum=MA6061T6.
[7]Nominal JC model parameters taken from Rule et al. (1997).

determining the peak shock pressure, but also morphologic parameters such as crater profile. iSALE simulations at 10 cppr are available for the first 7 experimental time steps. To reach a later stage of the experiment, a new calculation was performed at a resolution of 5 cppr. The overlapping 7 time steps are shown in Fig. 9. The crater profile from the lower resolution run is systematically smaller than that of the higher resolution. On average, radius estimates from the 5 cppr resolution simulation underestimate the experimental values by about 11%, while crater depth estimates underestimate experimental values by 14% (radii and depths estimated from the 5 cppr case are ~5% smaller than the values from the 10 cppr case). This clearly suggests that at a resolution of 5 cppr the mesh is under-resolved for the problem addressed here. As expected, a better fit is obtained with the 10 cppr resolution simulation, where both simulated radii and depths underestimate the experimental data on average by ~7% and 10%, respectively.

The effects of modeler choices on the simulation outcomes can be illustrated by the comparison of two independent CTH simulations for the glass-on-water experiment (KH = Keith Holsapple; DC = David Crawford). Fig. 10 shows resulting crater profiles and radius evolution with time, while the different CTH setups for the simulations in question are given in Table 5. The crater profiles for the two simulations are quite close, although variations are clearly visible at most time steps. The biggest difference occurs at the final time of 83.2 ms, where the KH simulation produces a significantly less concave profile than the impact experiment. Estimates of crater radius for the KH simulation tend to underestimate the experimental values during the first half of the resolution, and overestimate them during the second half, with oscillations of around 10%. Given that the late times quarter space experiment tends to underestimate the 'true crater' size by about 10%, the KH simulation appears to estimate the crater size quite closely. Estimates of crater radius for the DC simulation tend to consistently underestimate the experimental values by at most 5%, which corresponds to a slightly larger value when the 'true crater' size is taken into account. Resolution does not appear to play

Table 5. Summary of various shock codes set up for the glass-on-water impact simulations (*r* and *z* stand for horizontal and vertical resolution).

Code	Simulation type	EoS	Mesh size	Resolution (cppr)	Boundary conditions	Atmosphere in model	Profile determination
ALE3D	3D	Water: LEOS Table Glass: Hugoniot	*r*: 0 to 15 cm *z*: –5 to 15 cm	10	Pressure-continuous, non-reflecting	NO	Material boundaries
AUTODYN	2D(SPH)	Polynomial EoS Water: material library (ρ = 0.998 g/cm^3) Glass: material library for 'Float Glass B' (ρ = 2.05 g/cm^3)	*r*: 0 to 3 cm *z*: –3 to 2 cm	20 (pppr)[1]	Rigid (reflecting)	NO	Hand-picked using a density image
CTH (DC)	2D	MGRUN	*r*: 0 to 30 cm *z*: –30 to 30 cm	AMR: 10 zones (highest: 0.0375 cm; lowest: 0.6 cm)	Bottom: rigid Top/Sides: sound speed absorbing	NO	Density cut off: 0.5 g/cm^3
CTH (KH)	2D	SESAME	*r*: 0 to 25 cm *z*: –25 to 5 cm	AMR: 10 zones (highest: 0.078 cm; lowest: 0.25 cm)	Bottom/Sides: rigid	NO	Material boundaries
RAGE	2D	Water: SAIC EoS Glass: SESAME 2381	*r*: 0 to 36.48 cm *z*: –23 to 21.8 cm	20	Rigid (reflecting)	NO	Density cut off: 0.5 g/cm^3
iSALE	2D	Water: Tillotson Glass: wet tuff with ρ = 2.03 g/cm^3	*r*: 0 to 30.9 cm (low) 0 to 15.4 cm (high) *z*: –30.1 to 6.2 cm (low) –15.6 to 3.1 cm (high)	5 (low) 10 (high)	Top: outflow Bottom: no slip Sides: free slip	NO	Density cutoff: 0.1 g/cm^3
SOVA	3D	ANEOS Table for water and quartz	*r*: 0 to 3 cm (to 0.27 ms) 0 to 6 cm (>0.27ms) *z*: –3 to 1 cm (to 0.27 ms) –6 to 2 cm (>0.27 ms)	10 (to 0.27 ms) 5 (>0.27 ms)	Outflow	NO	Density cutoff: 0.8 (and 0.5) g/cm^3
ZEUS-MP2	2D	Water: Tillotson Glass: water Tillotson, with radius increased to match mass (r = 0.135 mm)	*r*: 0 to 38 cm *z*: –23 to 15 cm	7 near center (1.02 increase outward)	Bottom/Sides: rigid reflecting Top: outflow	YES	Density cutoff: 0.5 g/cm^3

[1]pppr = particles per projectile radius. This corresponds to SPH particles of 0.1 mm diameter.

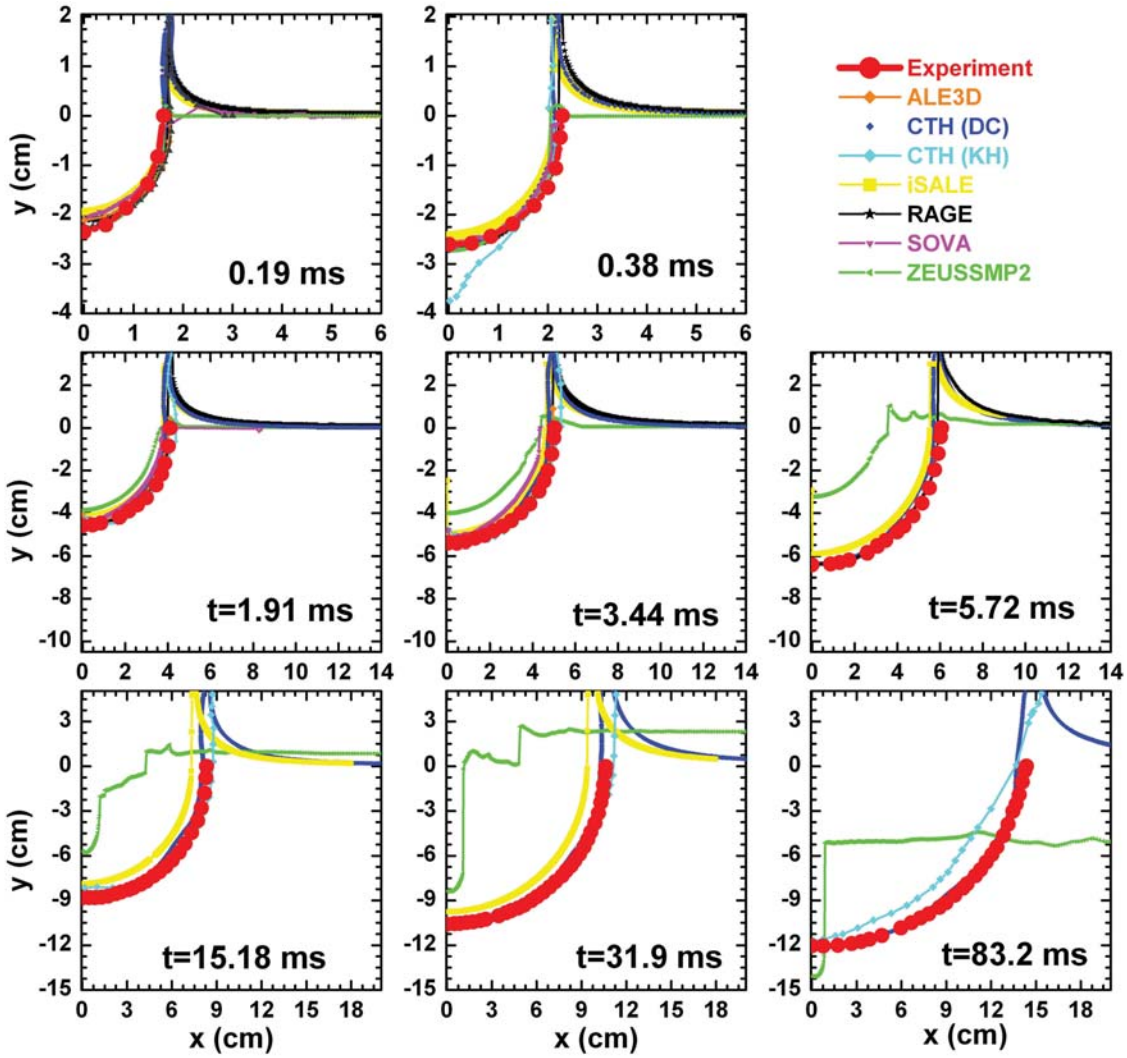

Fig. 7. Crater profiles at various stages of impact for the impact of a glass sphere on water estimated by the different codes compared to the measured experimental profiles.

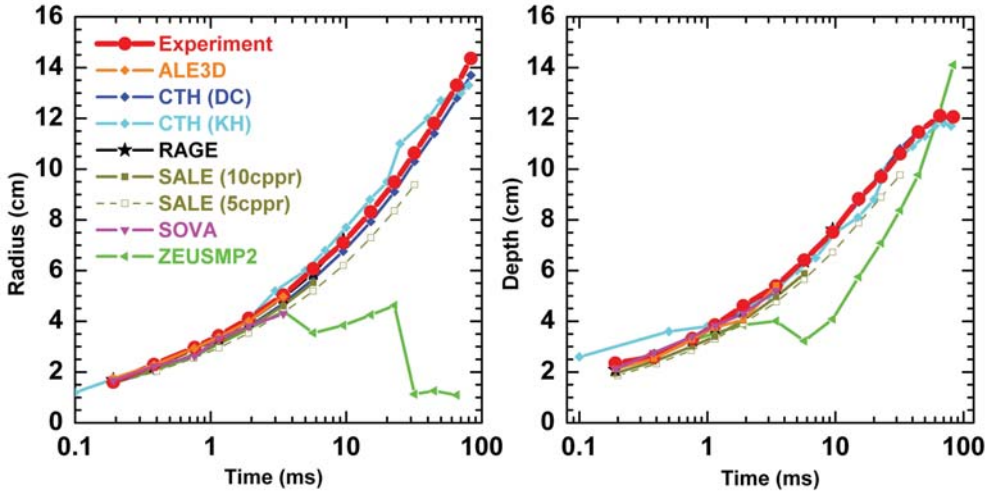

Fig. 8. Temporal evolution of crater radius and depth for the impact of a glass-on-water experiment estimated by the different codes compared to the experimentally determined ones.

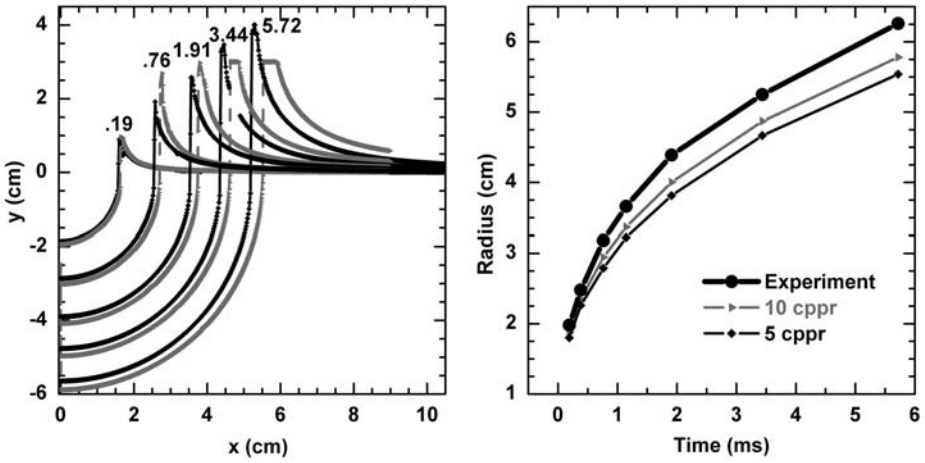

Fig. 9. Left: Crafter profiles at various time steps (in ms) from iSALE simulations with two different resolutions (5, black, and 10, gray, cppr) of the glass-on-water experiment. Right: Temporal evolution of the estimated radius from iSALE simulations (solid black and gray lines) compared to the experimental results (thick black line and dots).

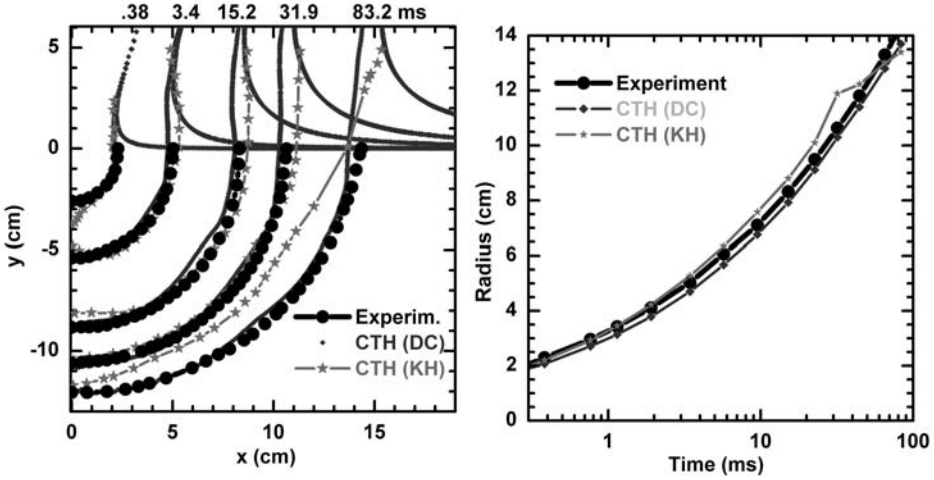

Fig. 10. Left: Crafter profiles at various times from CTH simulations carried out by two modelers (different model setup; "DC", and "KH") of the glass-on-water experiment. Right: Temporal evolution of the estimated radius from the two CTH simulations (solid dark and light gray lines) compared to the experimental results (thick black line and dots).

a major role, as both simulations are carried out with comparable resolution (both using AMR); however, the growing differences between the simulations at late time may result from different AMR refinement strategies chosen by KH and DC. A potentially important difference in the early time results is from the use of different equations of state for water (SESAME versus MGRUN). Profile determination is also different for the two simulations. The KH simulation used the CTH "high-resolution" interface tracker option (available in 2D), while DC opted for a more general approach (that can also be used in presence of vapor) based on a density of 0.5 g/cm^3. However, the low impact velocity of this test (no significant vapor production) guarantees that the two approaches are equivalent. Overall, however, both simulations appear to provide good estimates (with differences contained within ~10%) of crater radius and depth over time.

Validation #2: Aluminum-into-Aluminum

For this test we chose two alloys, 1100-O, which has a strain rate dependent strength, and 6061-T6, whose strength is insensitive to strain rate. Four code results are available at this time for Al 6061-T6 and Al 1100-O targets. Each simulation has been carried out with varying resolution (from AMR in CTH to 10 cppr in RAGE and AUTODYN) and varying strength model (simple von Mises criterion, Johnson-Cook, Steinberg-Guinan; see Appendix), as summarized in Table 6.

Overall, the code results are in relatively good agreement with the experimental data. For the impacts into Al 6061-T6 targets the numerical codes tend to slightly underestimate (5 to 13%) the crater radius and overestimate (4 to 12%) the crater depth, as shown in Fig. 11. For impacts into an Al 1100-O target, Fig. 12, code results are closer to experimental values. The codes underestimate crater radius by no more

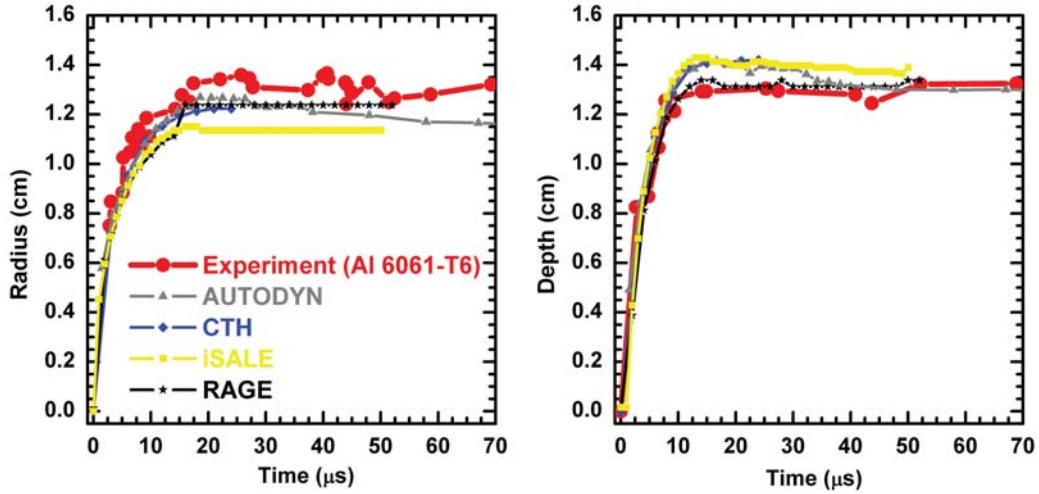

Fig. 11. Various codes' estimates of temporal evolution of crater radius and depth for the impact of an aluminum projectile on a target made of Al 6061-T6 compared to the experimental data.

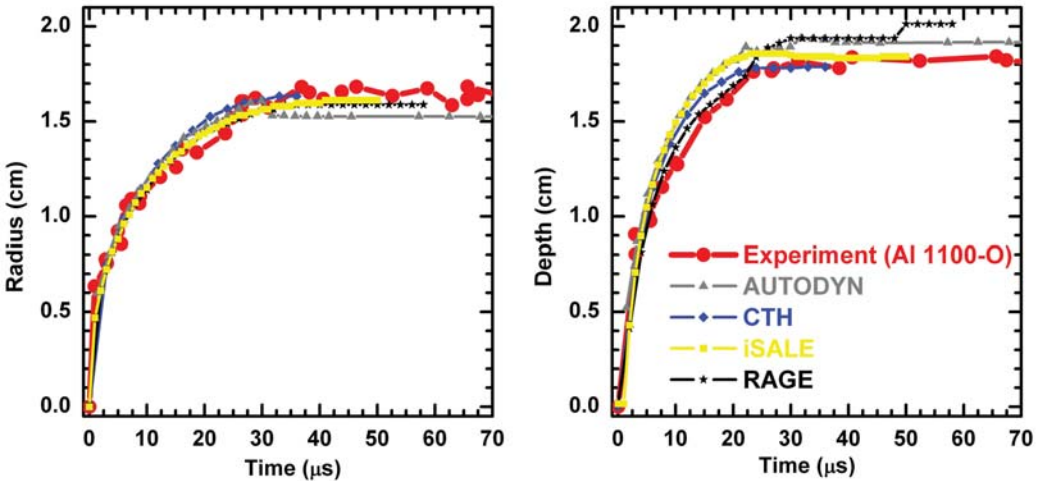

Fig. 12. Temporal evolution of crater radius and depth for the impact of an aluminum projectile on a target made of Al-1100, estimated by different codes compared to the experimental data.

than 6% and overestimate crater depth by no more than 8% (with the exception of the CTH simulation, that underestimates crater depth by about 1%). Note however that the experiments were in a relatively small sample, only a few times the crater size, which may have allowed a larger crater (see below).

Intra-Code Variability

Initial material model setup was investigated with iSALE simulations of Al 6061-T6 and CTH simulations of aluminum on Al 1100-O. Figure 13 shows three separate CTH simulations. The first simulation, the "reference" test, uses a full strength model for Al 1100-O with a strain-rate dependent strength and an "infinite target" (i.e., extending over 50 cm). A second simulation (small target ST) includes the full strength model but limits the target to a width of 5 cm, to investigate how the target size may affect the simulation's outcome. The small target case shows the largest discrepancy in crater radius estimate from the experimental data, close to 20%. The crater depth does not seem to have reached a plateau by the end of the simulation (when crater depth overestimates the experimental value by about 1%), which makes it hard to compare to the experimental test. The deterioration in simulation outcomes may be related to numerical effects associated with model boundary conditions. The importance of boundary effects was also emphasized in the water impact validation test. SOVA simulations show that when the edge of the crater gets close to the mesh boundary, crater size becomes significantly underestimated. A third simulation was run with CTH to test the importance of strain rate effects in the strength model. The results show that with a simplified strength model, i.e., without the strain rate dependence, the CTH results overestimate crater radius and depth, although by no more than 10 to 15%.

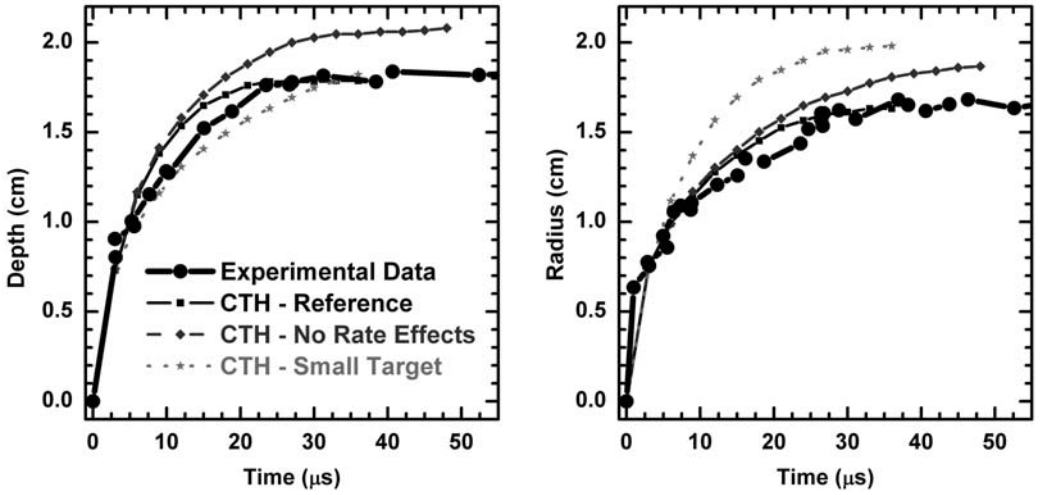

Fig. 13. Temporal evolution of crater radius and depth for the impact of an aluminum projectile on a target made of Al-1100, estimated by CTH with different initial setups compared to the experimental data.

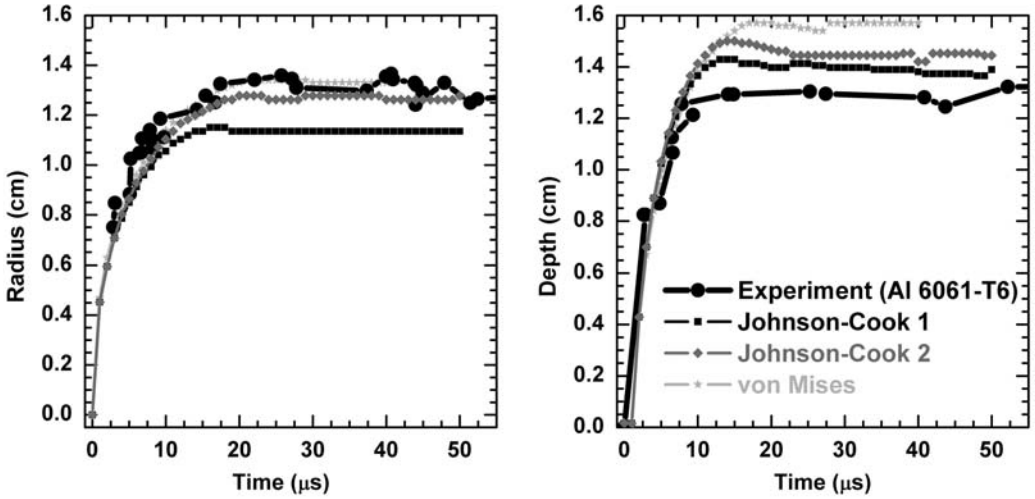

Fig. 14. Temporal evolution of crater radius and depth for the impact of an aluminum projectile on a target made of Al-6061, estimated by iSALE with the von Mises strength model and the Johnson-Cook model with two different values for Al 6061-T6 compared to the experimental data.

The sensitivity of the calculated crater dimensions to the choice of strength model is illustrated by a set of iSALE simulations of the impact into Al 6061-T6. One simulation used a simple von Mises model, with a typical shear strength for Al 6061-T6; two further simulations used the Johnson-Cook model with different parameters (see Table 6). The first set of Johnson-Cook model parameters (JC1), also used in the CTH simulation, was obtained from fits to experimental data in Benck et al. (1976), the second set (JC2) was taken from Rule et al. (1997). The results of these three simulations are shown in Fig. 14. The JC1 model is in closest agreement with the experiment in terms of depth (7.5% error), but underestimates the crater radius by ~13%; the von Mises model is in closest agreement with the experiment in terms of radius (1.2% error), but overestimates the crater depth by ~20%. The JC2 model provides the best compromise: it underestimates the crater radius by ~3.5% and overestimates crater depth by ~12%. In each case, the simulated crater depth is larger than the experiment. Overall, the range of the three model results is of the same magnitude as the discrepancy in crater dimensions between the models and the experiment.

SUMMARY

We present results from the first phase of a project to benchmark and validate shock codes used to simulate impact and explosion cratering. A variety of 2D and 3D codes were used in this study, from commercial products like AUTODYN, to codes developed within the scientific community like SOVA, SPH, ZEUS-MP, iSALE, and codes developed at National Laboratories like CTH, SAGE/RAGE, ALE3D.

We performed simple benchmark tests to compare the ability of each code to calculate shock wave propagation and decay in vertical and 45 degree impacts of 1km diameter, spherical aluminum projectiles into a aluminum half-space at both 5 km/s and 20 km/s. Strength was neglected in these simulations. The main conclusions from these initial tests are:

1. Variability in code results is to be expected due to differences in: the underlying solution algorithm of each code; artificial stability parameters; spatial and temporal resolution; and material models.
2. Shock pressure variability from code to code is within 8% for the 20 km/s impact simulations and 15% for the 5 km/s simulations.
3. The simulated peak shock pressure at a given distance from the point of impact depends on the number of cells used to resolve the projectile. For sufficiently high resolution, the numerical results converge on a solution; as resolution is decreased the pressure is increasingly underestimated. In general, a resolution of 20 cppr (cells per projectile radius) or higher is sufficient to calculate peak shock pressure to within 10% of the true (high-resolution) value.
4. Significant variability occurs due to code setup. It is important for users to understand the effects of internal code setup such as temporal and spatial stability parameters (Courant number or artificial viscosity).

In addition to benchmark tests, three validation tests were performed to examine the ability of codes to reproduce the time evolution of crater radius and depth observed in laboratory impacts in water and two well-characterized aluminum alloys. The main conclusions from the validation tests are:

1. The codes tested were in good agreement with experiments for impacts in water (no strength) and aluminum (well-characterized strength). Overall, model results are within 15–20% of experiments.
2. Model results of crater radius (and depth) as a function of time are within 10% of experiments (may be slightly larger for the water experiment, where the quarter-space set up tends to underestimate crater size by about 10%, at least at late times). This discrepancy is of approximately the same magnitude as the discrepancy due to code setup (modeler's choice) or to using alternative strength models for aluminum.
3. Some large discrepancies between models were observed. In each case these were associated with problematic initial or boundary conditions and in most cases, new simulations with improved initial conditions provided results in better agreement with the experiments.
4. Spatial resolution also affects a code's ability to simulate crater formation. In our tests, a resolution of 10–20 cppr was required to compute crater depth and radius to within 10% of the experimentally observed values. The effect of resolution is most significant in cases where the final crater is much larger than the projectile.
5. There appears to be a general tendency of shock codes to underestimate the radius of the forming crater, even accounting for the effect of resolution. Estimates of crater depth vary, from a tendency to underestimate it in the water test and overestimate it in the aluminum tests.

This study considers liquid water and metal. Liquid water can be modeled with zero strength, and common metals have simple and well measured strength models. The next phase of this project will address the validation of impact shock codes for the simulation of cratering in geologic materials, such as soils and rocks. In that case, benchmark and validation tests may be affected by limitations in material models, both equations of state and strength models, which are not well developed for geologic materials. This manuscript is PSI Contribution no. 449.

Acknowledgments–This work is supported by grants: NNX06AD65G (NASA), WU 355/5-2 (DFG), DNE/B501871/1 and NE/E013589/1 (NERC). We are grateful for the continued support for this work from other members of the cratering community, in particular, Galen Gisler, Boris Ivanov, Jay Melosh, and Elizabeth Turtle. The manuscript was much improved thanks to the detailed and very helpful comments from reviewers Alex Deutsch and Sarah Stewart and associate editor Gordon Osinski.

Editorial Handling—Dr. Gordon Osinski

REFERENCES

Ahrens T. J. and O'Keefe J. D. 1977. Equations of state and impact-induced shock-wave attenuation on the Moon. In *Impact and explosion cratering*, edited by Roddy D. J., Pepin R. O., and Merrill R. B. New York: Pergamon Press. pp. 639–656.

Amsden A. A., Ruppel H. M., and Hirt C. V. 1980. SALE: A simplified ALE computer program for fluid flow at all speeds. Los Alamos National Laboratories Report LA-8095. 101 p.

Amsden A. A. and Ruppel H. M. 1981. SALE-3D: A Simplified ALE Computer Program for Calculating Three-Dimensional Fluid Flow. Los Alamos National Laboratories Report LA-8905. 146 p.

Anderson C. E., Jr. 1987. An overview of the theory of hydrocodes. *International Journal of Impact Engineering* 5:33–59.

Benck R. F., Filbey G. L. Jr., and Murray E. A. Jr. 1976. Quasi-static compression stress-strain curves—IV, 2024-T3510 and 6061-T6 aluminum alloys. BRL Memorandum Report 2655. USA Ballistic Research Laboratories, Maryland.

Benz W. and Asphaug E. 1994. Impact simulations with fracture. I. Method and tests. *Icarus* 107:98–116.

Benz W. and Asphaug E. 1995. Simulations of brittle solids using smooth particle hydrodynamics. *Computer Physics Communications* 87:253–265.

Bjorkman M. D. and Holsapple K. A. 1987. Velocity scaling impact melt volume. *International Journal of Impact Engineering* 5: 155–163.

Carroll M. M. and Holt A. C. 1972. Static and dynamic pore-collapse relations for ductile porous materials. *Journal of Applied Physics* 43:1626–1636.

Century Dynamics, Inc. 2003. *AUTODYN Theory Manual 4.3*.

Collins G. S., Melosh H. J., and Ivanov B. A. 2004. Damage and deformation in numerical impact simulations. *Meteoritics & Planetary Science* 39:271–231.

Corey E. M. and Young D. A. 1998. A new prototype equation of state data library, Shock Compression of Condensed Matter–1997, 43–46.

Elbeshausen D., Wünnemann K., and Collins G. S. 2007. Three-dimensional numerical modeling of oblique impact processes: scaling of cratering efficiency (abstract #1952). 38th Lunar and Planetary Science Conference. CD-ROM.

Gault D. E. and Sonett C. P. 1982. Laboratory simulations of pelagic asteroidal impact: Atmospheric injection, benthic topography, and the surface wave radiation field. In *Geological implications of impacts of large asteroids and comets on the Earth*, edited by Silver L.T. and Schultz P. H. GSA Special Paper 190. pp. 69–92.

Gingold R. A. and Monaghan J. J. 1977. Smoothed particle hydrodynamics—Theory and application to non-spherical stars. *Monthly Notes of the Royal Astronomical Society* 181:375–389.

Gittings M. L. 1992. SAIC's Adaptive grid Eulerian hydrocode. Defense Nuclear Agency Numerical Methods Symposium, 28–30 April 1992.

Grady D. E. and M. E. Kipp 1980. Continuum modelling of explosive fracture in oil shale. *International Journal of Rock Mechanics and Mineral Science & Geomechanics Abstracts* 17:147–157.

Hayes J. C., Norman M. L., Fiedler R. A., Bordner J. O., Li P. S., Clark S. E., ud-Doula A., and Mac Low M.-M. 2006. Simulating radiating and magnetized flows in multiple dimensions with ZEUS-MP. *The Astrophysical Journal (Supplement*) 165:188–228.

Herrmann W. 1969. Constitutive equation for the dynamic compaction of ductile porous material. *Journal of Applied Physics* 40:2490–2499.

Holsapple K. A. 2008. On the "strength" of the small bodies of the solar system: A review of strength theories and their implementation for analyses of impact disruptions. *Planetary and Space Science*, doi:10.1016/j.pss.2008.05.015.

Ivanov B. A. 2005. Shock melting of permafrost on Mars: Water ice multiphase equation of state for numerical modeling and its testing (abstract #1232). 36th Lunar and Planetary Science Conference. CD-ROM.

Ivanov B. A. and Kostuchenko V. N. 1997. Block oscillation model for impact crater collapse (abstract #1655). 27th Lunar and Planetary Science Conference. CD-ROM.

Ivanov B. A., Deniem D., and Neukum G. 1997. Implementation of dynamic strength models into 2D hydrocodes: Applications for atmospheric breakup and impact cratering. *International Journal of Impact Engineering* 20:411–430.

Ivanov B. A., Langenhorst F., Deutsch A., and Hornamann U. 2002. How strong was impact-induced CO_2 degassing in the Cretaceous-Tertiary event? Numerical modeling of shock recovery experiments. In *Catastrophic events and mass extinctions: Impacts and beyond*, edited by Koeberl C. and MacLeod K. G. GSA Special Paper 356. pp. 587–594.

Johnson G. R. and Cook W. H. 1983. A constitutive model and data for metals subjected to large strains, high strain rates and high temperatures. Proceedings, 7th International Symposium on Ballistics. Hague, The Netherlands.

Johnson G. R. and Holmquist T. J. 1994. An improved computational model for brittle materials. In *High-pressure science and technology—1993*, edited by Schmidt S. C., Shaner J. W., Samara G. A., and Ross M. Woodbury, NY: AIP Press. pp. 981–984.

Kerley G. I. 1989. Equations of state and gas-gas separation in soft-sphere mixtures. *Journal of Chemical Physics* 91:1204–1210.

Kerley G. I. 1991. User's manual for PANDA II: A computer code for calculating equations of state. Sandia National Laboratories Report SAND88-2291.

Korycansky D. G., Zahnle K. J., and MacLow M.-M. 2000. High resolution simulations of the impacts of asteroids into the Venusian atmosphere. *Icarus* 146:387–403.

Korycansky D. G., Zahnle K. J., and MacLow M.-M. 2002. High resolution simulations of the impacts of asteroids into the Venusian atmosphere 2: 3D Models. *Icarus* 157:1–23.

Korycansky D. G. and Zahnle K. J. 2003. High resolution simulations of the impacts of asteroids into the Venusian atmosphere III: Further 3D Models. *Icarus* 161:244–261.

Lucy L. 1977. A numerical approach to the testing of the fission hypothesis. *Astronomical Journal* 82:1013–1024.

Lundborg N. 1968. Strength of rock-like materials. *International Journal of Rock Mechanics and Mineral Science* 5:424–454.

Lyon S. P. and Johnson J. D. 1992. SESAME: The LANL equation of state database. Los Alamos National Laboratories Report LA-UR-92-3407.

Malin M. C., Edgett K. S., Posiolova L. V., McColley, S. M., and Noe Dobrea E. Z. 2006. Present-day impact cratering rate and contemporary gully activity on Mars. *Science* 314:1573–1577.

McClintock F. and Argon A., eds. 1966. *Mechanical behaviour of materials*. Reading: Addision-Wesley. p. 326 and Ch. 5.

McGlaun J. M., Thompson S. L., and Elrick M. G. 1990. CTH: A three-dimensional shock wave physics code. *International Journal of Impact Engineering* 10:351–360.

Melosh H. J. 1979. Acoustic fluidization: A new geologic process? *Journal of Geophysical Research* 84:7513–7520.

Melosh H. J. 1989. *Impact cratering: A geologic process*. New York: Oxford University Press. 245 p.

Melosh H. J. 2000. A new and improved equation of state for impact computations (abstract #1903). 31st Lunar and Planetary Science Conference 31. CD-ROM.

Melosh H. J. 2007. A hydrocode equation of state for SiO_2. *Meteoritics & Planetary Science* 42:2079–2098.

O'Keefe J. D., Stewart S. T., Lainhart M. E., and Ahrens T. J. 2001. Damage and rock-volatile mixture effects on impact crater formation. *International Journal of Impact Engineering* 26:543–553.

Pierazzo E. and Melosh J. H. 2000. Melt production in oblique impacts. *Icarus* 145:252–261.

Pierazzo E., Vickery A. M., Melosh H. J. 1997. A reevaluation of impact melt production. *Icarus* 127:408–423.

Prater R. 1970. Hypervelocity impact—Material strength effects on crater formation and shock propagation in three aluminum alloys. Technical Report AD0718461.

Rule W. K. 1997. A numerical scheme for extracting strength model coefficients from Taylor test data. *International Journal of Impact Engineering* 19:797–810.

Schmidt R. M. and Housen K. R. 1987. Some recent advances in the scaling of impact and explosion cratering *International Journal of Impact Engineering* 5:543–560.

Senft L. E. and Stewart S. T. 2008. Impact crater formation in icy layered terrains on Mars. *Meteoritics & Planetary Science* 43. This issue.

Sharp R. 2004. Users manual for ALE3D. UCRL-MA-152204 Rev. 1.

Shuvalov V. V. 1999. Multi-dimensional hydrodynamic code SOVA for interfacial flows: Application to the thermal layer effect. *Shock Waves* 9:381–390.

Stacey F. D. 1977. *Physics of the Earth*, 2nd ed. London: Wiley and Sons. 414 p.

Steinberg D. J. 1996. Equation of state and strength properties of selected materials. Lawrence Livermore National Laboratory Report UCRL-MA-106439.

Steinberg D. J., Cochran S. G., and Guinan M. W. 1980. A constitutive model for metals applicable at high strain rates. *Journal of Applied Physics* 51:1498–1504.

Swesty X. 1996. Thermodynamically consistent interpolation of EoS tables. *Journal of Computational Physics* 127:118–127

Thompson S. L. 1970. Improvements in the CHART D radiation-hydrodynamic code I: Analytical equation of state. Sandia National Laboratories Report SC-RR-70–28.

Thompson S. L. and Lauson H. S. 1972. Improvements in the Chart-D radiation hydrodynamic code III: Revised analytical equation of state. Sandia National Laboratories Report SC-RR-710714.

Tillotson J. H. 1962. Metallic equations of state for hypervelocity impact. San Diego: Gen. At. Report GA-3216.

Wünnemann K., Collins G. S., and Melosh H. J. 2006. A strain-based porosity model for use in hydrocode simulations of impacts and implications for transient-crater growth in porous targets, *Icarus* 180:514–527.

APPENDIX

Strength Models for Aluminum

Three strength models have been used by codes to simulate the response of aluminum to deformation. They use the invariant measure of the deviatoric stress tensor as the "effective" or "equivalent" stress:

$$\sigma_{EQ} = \sqrt{\frac{3}{2} s_{ij} s_{ij}} = \sqrt{3 J_2}, \quad \text{(A1)}$$

where s_{ij} is the deviatoric stress tensor and J_2 is the second invariant of the deviatoric stress tensor. This expression conveniently reduces to $\sigma_{EQ} = \sigma_1$ in the case of uniaxial compression or tension, thus allowing experimental uniaxial stress-strain data to be used directly to define the yield strength.

The simplest choice of strength model is to define the yield strength as a constant $Y = Y_{vm}$; this is often referred to as the *von Mises yield criterion*. The *Johnson-Cook strength model* for metals subjected to large strains, high strain rates and high temperatures (Johnson and Cook 1983) is defined as

$$Y = (A + B\varepsilon^n)(1 + C\ 1n\dot{\varepsilon})\left[1 - \left(\frac{T - T_{rf}}{T_m - T_{rf}}\right)^m\right], \quad \text{(A2)}$$

where ε is the equivalent plastic strain ($\varepsilon = \int \sqrt{2 d\varepsilon_{ij}^p d\varepsilon_{ij}^p / 3}$, where $d\varepsilon_{ij}^p$ is the deviatoric plastic strain increment tensor), $\dot{\varepsilon} = \sqrt{2\dot{\varepsilon}_{ij}\dot{\varepsilon}_{ij}/3}$ is the strain rate, and T is temperature. The model is defined by 6 constants: A (the yield strength at the reference state; $T = T_{rf}$, $\varepsilon = 0$, $\dot{\varepsilon} = 1$), B, C, n, m, T_{rf} (reference state temperature) and T_m (the melt temperature). (Note the discrepancy between assuming thermal degradation at a fixed temperature rather than with some comparison to the pressure-dependent melt temperature). The *Steinberg-Guinan strength model* for metals at high strain rates (Steinberg et al. 1980) defines both the shear modulus G and shear strength Y, as functions of pressure p, temperature and equivalent plastic strain, but neglects strain rate dependence:

$$G = G_0\left[1 + \frac{G'_p}{G_0}\frac{p}{n^{1/3}} + \left(\frac{G'_T}{G_0}\right)(T - 300)\right], \quad \text{(A3)}$$

$$Y = \min Y_0(1 + \beta(\varepsilon + \varepsilon_i)^n), Y_{\max} \left[1 + \frac{Y'_p}{Y_0}\frac{p}{\eta^{1/3}} + \left(\frac{G'_T}{G_0}\right)T - 300\right], \quad \text{(A4)}$$

In these equations, η is compression (ρ/ρ_0), β and n are work-hardening parameters, and ε_i is the initial equivalent plastic strain (normally equal to zero). The subscript "0" refers to the reference state ($T = 300$ K, $p = 0$, $\varepsilon = 0$). Primed parameters with the subscripts p and T imply derivatives of that parameter with respect to pressure or temperature at the reference state. Note that implicit in Equation A4 is the assumption that $Y'_T/Y_0 = G'_T/G_0$, which is required for self consistency (McClintock and Argon 1966).